2024 IEEE/RSJ International Conference on Intelligent Robots and Systems (IROS)
October 14-18, 2024. Abu Dhabi, UAE

2024 IEEE/RSJ International Conference on Intelligent Robots and Systems (IROS) | 979-8-3503-7770-5/24/$31.00 ©2024 IEEE | DOI: 10.1109/IROS58592.2024.10802223

A Novel Variable Stiffness Suspension System for Improved Stability and Control of Tactile Mobile Manipulators

Sebastian Kuhn[1], Mehmet C. Yildirim[*,1], Edmundo Pozo Fortunić[1], Kübra Karacan[1], Abdalla Swikir[1,2], and Sami Haddadin[1]

***Abstract*— Mobile manipulators (MM) have proven valuable in assisting humans in industrial settings. However, their strict separation from humans in controlled environments limits their effectiveness. Efforts have been made to bridge this gap for physical human-robot interaction (pHRI), leading to the development of collaborative mobile manipulators (CMM). Nonetheless, unpredictable environments continue to present challenges. This paper introduces an innovative suspension design for mobile bases (MBs) to enhance the safety and autonomy of CMMs. We propose an electromechanical approach leveraging variable stiffness and combining passive springs with adaptive transmission mechanisms. Through simulation, physical prototype development, and experimental validation, we demonstrate the effectiveness of our approach in stabilizing the MB against external disturbances. Our findings provide valuable insights for the development of CMMs in dynamic environments.**

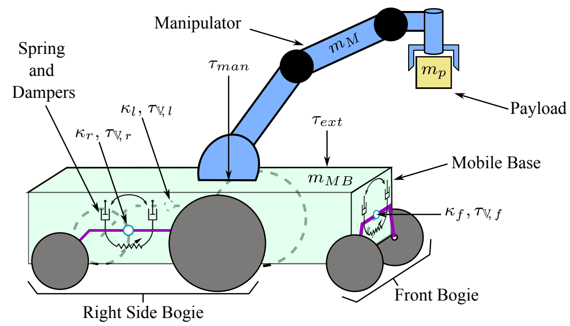

Fig. 1. Concept sketch of a future wheeled mobile manipulator (MM) with payload and the proposed variable-stiffness suspension model shown on the bogie mechanisms.

I. Introduction

Enabling robots to function alongside humans as co-workers is a pivotal goal in modern robotics research [1]. Mobile manipulators (MM), which integrate manipulator dexterity with mobile robot extensive workspace, have demonstrated their value in industrial settings [2]–[5]. However, a significant drawback of current MM applications is that they perform their operation in isolated, controlled environments, as detached from human interaction, thereby limiting their potential effectiveness. Efforts to bridge the gap between humans and robots have created collaborative mobile manipulators (CMMs). These systems integrate vision and force control, enabling partial adaptation to various environments and facilitating safe coexistence with humans [6], [7]. However, transitioning from traditional MMs to CMMs only partially addresses the challenges, especially in direct physical human-robot interaction (pHRI). The advancement in this domain has led to the emergence of a sub-domain: the tactile mobile manipulator (TMM, see Fig. 1). These are explicitly designed for pHRI tasks such as: assisting humans in object handling [8] and interacting with the environment through tactile interactions (e.g. opening doors)[9]. Despite these advancements, TMMs encounter significant challenges when they enter environments that are designed while considering only humans. Although in daily life, ground artefacts like small steps, ramps, impurities, foreign objects, etc., are not even recognized as challenging by a human, they create an unpredictable operational environment for TMMs, particularly concerning their mobile bases (MB) [10].

Ensuring passive safety under such unpredictability is paramount to developing TMMs, particularly given their proximity to humans. Passive safety precautions necessitate an overall reduction in the mass of the TMM (m_{TMM}) to minimize impact energy during interactions [11], [12]. Manipulator's (m_M) and MB's (m_{MB}) masses are the main contributors to the m_{TMM} and as depicted in Fig. 2 the majority of this mass comes from the m_{MB}. Consequently, the trend towards mass reduction in traditional MMs must extend to the mobile bases of future TMMs [3], [13], [14]. On the other hand, despite the drive towards lighter structures, it remains essential for future TMMs to have a payload m_p capacity at least equal to the capacities of current CMMs on the market. Based on these points, we came up with a conceptual future TMM, shown in Fig. 2, which should have a lower total mass while the relative m_p to m_{MB} is higher. Although the overall mass reduction addresses the safety issue for collision cases, another major point is the operational safety and long-term integrity of the TMM itself. A design guided by these factors necessitates the capability of navigating unpredictable obstacles on the ground while resisting the external forces τ_{ext} of human interaction and the forces generated by the motion of the manipulator τ_{man} [10]. With these aspects taken into consideration, it also shouldn't be ignored that the transition towards human-robot collaboration intensifies the demand for energy-efficient operation to enhance autonomy, and such a more efficient TMM system will also require smaller energy sources and less actuation power, which would eventually indirectly contribute to the mentioned passive safety aspect also.

This work was partially supported by the European Union's Horizon 2020 research and innovation programme as part of the projects Darko under grant no. 101017274 and ReconCycle under grant no. 871352, and partially supported by the funding of the Lighthouse Initiative KI.FABRIK Bayern, (Phase 1: Infrastructure as well as the research and development program under grant no. DIK0249), by the Bavarian State Ministry for Economic Affairs, Regional Development, and Energy (StMWi).

[1] All authors are with the Munich Institute of Robotics and Machine Intelligence (MIRMI), Technical University of Munich (TUM), 80992, Munich, Germany. e-mail: {se.kuhn}, {firstname.surname}@tum.de

[2] Abdalla Swikir is also with the Department of Electrical and Electronic Engineering, Omar Al-Mukhtar University (OMU), Albaida, Libya.

[*] is the corresponding author.

Solutions based on existing TMM architectures, as demonstrated in [9], could be explored to address these challenges. For example, leveraging manipulator redundancy to compensate for undesired base motions is a potential avenue. However, such approaches might increase power consumption and reduce manipulator control bandwidth. Alternatively, modifying the MB could offer a more suitable solution. Integrating a passive-compliant suspension system could yield significant benefits. Specifically, such a system could mitigate safety issues associated with navigating ground obstacles by effectively compensating for disturbances, thus enabling robust and energy-efficient operation. Nevertheless, conventional passive systems cannot adapt their characteristics [15], [16], which is essential for TMMs to accommodate payload changes and external forces, especially since our predictions show the gap between m_p and m_{MB} will be increasingly closed.

To address the adaptability issue, active suspension systems, which utilize electromechanical, hydraulic or pneumatic actuators to apply force directly to the wheels [17], can be considered. The stiffness variation method by using hydraulic and pneumatic has achieved success to compensating for changing mass [18], [19] and controlling the body's attitude [20], [21]. While the active suspension with stiffness variation approach can impose any desired motion with the highest bandwidth among adaptive options, due to its always-active nature, it also generally incurs the highest power consumption [22] relative to other types of adaptive suspensions. Alternatively, via the electromechanical approach, which introduces a variable transmission to the kinematic coupling between the suspension joints and the spring, attitude control for cars in [23]–[26] is achieved. This variable-transmission solution enables the adjustment of stiffness and output force at a low energy cost compared to the mentioned alternatives, and it allows further efficiency with semi-active application possibility, which is particularly appealing not only for the mentioned automotive but also for TMM applications.

This study presents a solution to the aforementioned challenges by introducing an adaptive semi-active suspension (SAS) system for TMMs. Drawing from established adaptive suspension designs and prioritizing passive safety enhancement, we propose integrating variable stiffness mechanisms into the suspension to stabilize the MB. Specifically, we employ an energy-efficient electromechanical method that combines passive springs with variable transmission systems. The effectiveness of our inventive adaptive suspension is validated through simulation and experimental testing and compared to a passive alternative. These results lay the foundation for enhancing the autonomy and safety of TMMs in dynamic and uncertain environments.

The structure of this article is as follows: In Section II, we offer a comprehensive description of the proposed suspension design and conduct a comparison with potential alternatives through simulation. Section III introduces the developed physical prototype for variable stiffness on a SAS system for TMMs, encompassing its mechanics, electronic components, and low-level control setup. Afterwards, Section IV outlines the experimental setup, procedure, and results validating the proposed concept before concluding the work in Section V.

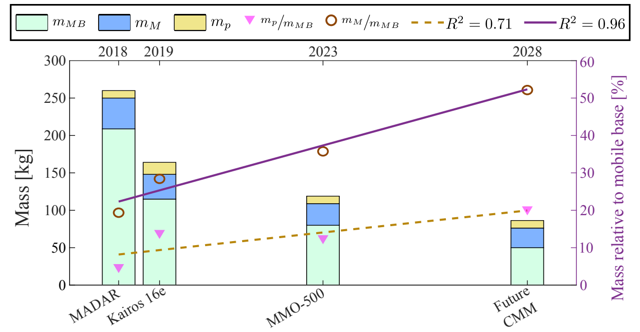

Fig. 2. Absolute and relative masses of the base (m_{MB}), manipulator (m_M), and payload (m_p) for three modern MM (see [3], [13], [14]) and a potential future system. The parameters of the latter were extrapolated from the existing MM's data, assuming a linear development over time.

II. Background

To further understand the effectiveness of the SAS and build up the necessary background information, we performed a simulation study. To accomplish this goal, we adopt the concept of variable mechanical stiffness, as outlined in previous studies such as [23]. Specifically, we utilize three independently powered variable stiffness systems (VSS) to control the roll, pitch, and heave degrees of freedom (DoF) of the MB.

A. Dynamic system model

The functionality of the proposed suspension is best understood through the task level, wherein the MM is conceptualized as a branched kinematic chain, with the MB body serving as the root body. Its dynamic behaviour can be manipulated using three independent variable stiffness systems (VSS,$\mathbb{V}$) with indices f, l, r corresponding to Front, Left, and Right, respectively. Their output angles (shown in Fig. 6 (c)) are part of the joint space $\boldsymbol{q} := \begin{bmatrix}\Phi_f & \Phi_l & \Phi_r & \boldsymbol{q_M}^\top\end{bmatrix}^\top$ in which $\boldsymbol{q_M} \in \mathbb{R}^{nx1}$ is the joint space of the manipulator and the dynamic model is written as:

$$\boldsymbol{M}\ddot{\boldsymbol{q}} + \boldsymbol{C}\dot{\boldsymbol{q}} + \boldsymbol{K}(\boldsymbol{q},\boldsymbol{u})\boldsymbol{q} + \boldsymbol{g}(\boldsymbol{q}) = \boldsymbol{\tau}_{\mathbb{V}}(\boldsymbol{q},\boldsymbol{u}) + \boldsymbol{\tau}_{dist}(t), \quad (1)$$

$$\boldsymbol{\tau}_{dist}(t) = \boldsymbol{\tau}_{man}(t) + \boldsymbol{\tau}_{ext}(t)\,. \quad (2)$$

Therein, the matrices $\boldsymbol{M}$, $\boldsymbol{C}$, $\boldsymbol{K} \in \mathbb{R}^{3x(3+n)}$ represent the inertia, damping, and stiffness of the system, respectively. As the payload inertia $\boldsymbol{M}_P(\boldsymbol{q},t) \geq \boldsymbol{0}$ may change during operation, the vector of total gravity $\boldsymbol{g}(q)$and the total inertia matrix $\boldsymbol{M}(\boldsymbol{q},t)$ are time-dependent:

$$\boldsymbol{M}(\boldsymbol{q},t) = \boldsymbol{M}_{\mathrm{TMM}}(\boldsymbol{q}) + \boldsymbol{M}_P(\boldsymbol{q},t)\,. \quad (3)$$

Other pHRI-related disturbances are included in $\boldsymbol{\tau}_{dist}(t)$ in which $\boldsymbol{\tau}_{man}(t)$ represents the manipulator joint torques and $\boldsymbol{\tau}_{ext}(t)$ all other external forces projected into the joint space. The stiffness control (see II-C.1) compensates for $\boldsymbol{M}_P(\boldsymbol{q},t)$, $g(q)$ and $\boldsymbol{\tau}_{dist}(t)$ by adjusting the cart angles α that are included in the control output vector: $\boldsymbol{u} := \begin{bmatrix}\alpha_f & \alpha_l & \alpha_r\end{bmatrix}^\top$.

Those changes of $\boldsymbol{u}$ affect $\boldsymbol{K}$ as it contains the revolute stiffness of the three VSS but also the torque $\boldsymbol{\tau}_{\mathbb{V}}$ exerted on the joints by the VSS:[1]

$$\boldsymbol{K}(\boldsymbol{q},\boldsymbol{u}) := \boldsymbol{I}\begin{bmatrix}\kappa_f(\Phi_f,\alpha_f) & \kappa_l(\Phi_l,\alpha_l) & \kappa_r(\Phi_r,\alpha_r) & \boldsymbol{0}\end{bmatrix}^\top \quad (4)$$

$$\boldsymbol{\tau}_{\mathbb{V}}(\boldsymbol{q},\boldsymbol{u}) := \begin{bmatrix}\tau_{\mathbb{V},f}(\Phi_f,\alpha_f) & \tau_{\mathbb{V},l}(\Phi_l,\alpha_l) & \tau_{\mathbb{V},r}(\Phi_r,\alpha_r) & \boldsymbol{0}\end{bmatrix}^\top. \quad (5)$$

[1]Note that all equations in the remainder of the work are the same for each of the three VSS; therefore, f, l, r indices are omitted after this point.

B. Proposed suspension concept

The proposed suspension topology shown in Fig. 1 is based on the swing-arm suspension of the SAM robot [10]. Three hinges (blue) connect the six swing arms (purple) to the body, with the VSS (green) being located at the hinges, each connecting a pair of swing arms. This means that the system is compliant and the three VSS fully and non-redundantly controls the body pitch, roll and vertical DoF. Each swing arm is connected individually to the body through a fluid damper to ensure all movements are damped.

C. TMM Concept Modelling and Evaluation

The performance of the proposed suspension system and a passive alternative in the proposed TMM application are compared below. As the TMM itself has yet to be built, a detailed multi-body simulation (MBS) (Section II-C.3) is the basis for this evaluation. The different systems were modelled in the simulation as follows:

- **Passive suspension:** Only passive linear springs and dampers are used, and they are tuned such that a damping ratio of $\delta_p = 0.4$ and vertical eigenfrequency $\omega_{0,p}$ =2.3 Hz is achieved at no payload.
- **SAS:** The analytical simulation model of the proposed VSS (see Section II-C.3) is used together with passive dampers. The parameters are the same as those of the hardware prototype (Tab. II).

For each system, a drive across a 12 m section of the ground profile at a constant speed of $v_{TMM} = 0.5\,\mathrm{m/s}$ is simulated. The manipulator motion and external forces are also included in the simulation. The results of these simulations are used to define the required ranges of loading forces and frequencies to test the developed system.

*1) **Stiffness control**:* In the literature, stiffness control is applied to the roll and pitch motion [24], [27], [28] and additionally, the body heaves [25], [29] of cars. In all of these applications, though, the stiffness variation is only used as force control to compensate for disturbance forces, and for this purpose, linear controllers up to second order [24], [25], [27] as well as full-state feedback optimal control [29] and neural networks [25] are used. However, the stiffness control of the previously explained TMM application has to achieve not only the goal of external disturbance, such as exerted forces by the humans, forces generated by the task medium, and compensation via force control, but also that of reducing the effect of ground obstacle via position control of the TMM body, which, to the best of our knowledge, was never before done in the literature.

The control architecture for the TMM is structured to allow each of the three VSS to be independently controlled. This means that in the hardware setup (Section IV-A), the same controller is used as in the simulation, which is explained in the following. For deriving the control, a simplified linear model was developed based on the classic quarter-car model [30] that describes the dynamics of only one of the three joints. The core of this model is the linear VSS model, which is equivalent to the entire model given in Eq. 13 and III-B at all operating points but facilitates the use of linear control. In this architecture-level model, the torque and stiffness are determined by the constant preload parameters ς and γ (which are explained in Section III-B)

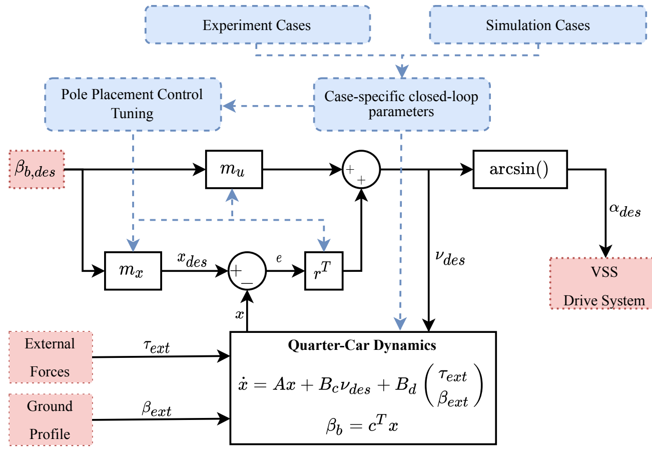

Fig. 3. Block diagram of the closed-loop joint stiffness control model. Elements related to the tuning are colored in blue, while connections to other system parts are labeled in red.

as well as the transmission ratio $\nu = sin(\alpha)$. As the control output is the desired transmission ratio ν_{des}, the actual ν follows it with a first-order delay with the time constant T_d, representing the actuation delay. Furthermore, the body motions caused by the deflection of the VSS joint are defined by the joint space angle β_b, while the wheel motions caused by the ground and the joint are represented by β_u. This means that:

$$\Phi = \beta_b - \beta_u \,. \tag{6}$$

The state space model that was built using the linearization is shown in Fig. 3, and its matrices and vectors are given in the following:

$$x = \begin{pmatrix} \beta_b \\ \dot{\beta}_b \\ \beta_u \\ \dot{\beta}_u \\ \nu \end{pmatrix}, B_c = \begin{pmatrix} 0 \\ 0 \\ 0 \\ 0 \\ \frac{1}{T_d} \end{pmatrix}, B_d = \begin{pmatrix} 0 & 0 \\ \frac{1}{J_b} & 0 \\ 0 & 0 \\ 0 & a_1 \\ 0 & 0 \end{pmatrix}, \tag{7}$$

$$A = \begin{pmatrix} 0 & 1 & 0 & 0 & 0 \\ -a_2 & -\frac{c_b}{J_b} & a_2 & \frac{c_b}{J_b} & -\frac{k_c}{J_b}\varsigma\gamma \\ 0 & 0 & 0 & 1 & 0 \\ a_3 & \frac{c_b}{J_u} & -[a_1 + a_3] & -\frac{c_b}{J_u} & \frac{k_c}{J_u}\varsigma\gamma \\ 0 & 0 & 0 & 0 & -\frac{1}{T_d} \end{pmatrix}, \tag{8}$$

with $a_1 = {}^{k_u}/_{J_u}$, $a_2 = {}^{R^2 k_c \nu_0^2}/_{J_b}$, and $a_3 = {}^{R^2 k_c \nu_0^2}/_{J_u}$ while J_b and J_u represent the body and wheel masses reflected β_b, β_u. Furthermore, k_t is the constant stiffness of the tyres reflected in the VSS joint, and c_b is the constant damping. Finally, ν_0 represents the transmission ratio and thus stiffness setting around which the linearization was done. The controller is a full-state feedback controller[31] that uses the feedback gain vector r and the feed-forward gain vectors m_u and m_x. The gain vectors were tuned for each testing case using MATLAB *systune* functionality with the pole placement tuning goal [32]. The closed-loop structure is also shown in Fig. 3.

*2) **Ground profile and environment**:* Understanding the environment that a TMM might operate in is the first step in designing a solution. Three critical elements of such an environment are explored in this work: The ground profile, external forces that could act on the system, and possible

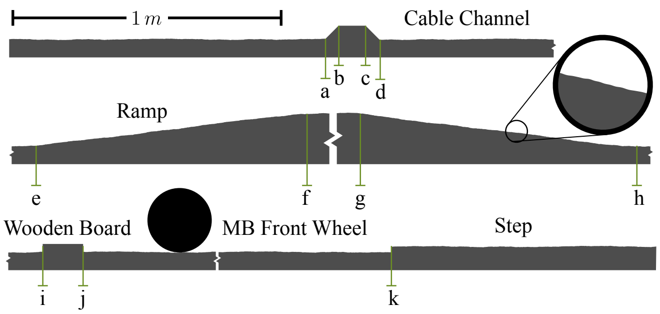

Fig. 4. Sections of the ground profile showing different obstacles that are present in the simulation's ground profile and the used TMM model's front wheel for size comparison.

payloads. The main focus is on the ground profile, as it is both a fundamental assumption for suspension design and evaluation and an unexplored area of research for TMM. It is assumed that a typical TMM will operate in warehouses, factories, and similar industrial environments where the ground is not obstacle-free but somewhat unpredictable.

As a starting point for defining the likely obstacles, the industrial standards for general concrete floors [33], worker safety [34], and barrier-free accessibility [35] were used. Assumptions about the typical environments were also made, leading to the obstacles shown in Fig. 4. Other than the shape of the obstacles, the texture of the surfaces also has to be modelled. For all surfaces except the smooth cable channel, the texture is defined by a class A surface according to the ISO 8608 industry standard [36], which represents a concrete surface according to [30]. This standard specifies a harmonic height profile Φ based on power spectral density measures. A significant difference between the TMM application and automotive applications of adaptive-stiffness suspensions [23]–[26] is that significant external forces can act on the MB, as explained before. Since the TMM concept requires the handling of payloads while driving, one type of force comes from the motion and acceleration of the manipulator and its payload. Therefore, the choice of inertial parameters for both is a crucial assumption explained below.

*3) **TMM Multi-Body Simulation Model:*** The MBS model was built using the software MSC.Adams (MSC Software Corporation) as a rigid-body model representing the body's main DoF, suspension, and manipulator. It uses the Fiala tyre model [37] included in Adams and the custom ground profile defined in Section II-C.2 to represent the tire-ground interaction. For the parametrization of the MB, the TMM base prototype SAM [10] is used. The MBS model shares its kinematics and inertial parameters as SAM was designed to support the Franka Robot tactile manipulator [38]. The payload carried by the manipulator is modelled as a cube of $200\,\mathrm{mm}$ edge length. Its mass and inertia parameters are scaled to adapt to the mass case (m_{MB}=71.00 kg, m_M=18.00 kg, m_p=4.97 kg) representing current and future development. Finally, interactions with the environment are described as an external force wrench F_{exz} that acts on the MB (see Section II-C.2).

The MBS model is coupled with a Simulink model using Co-Simulation. In this analytical model, the stiffness control (Section II-C.1) is modelled, and due to the Co-simulation with the Adams model, a closed loop is formed. The Simulink part of the simulation also includes a model of each VSS that accurately represents the mechanism of

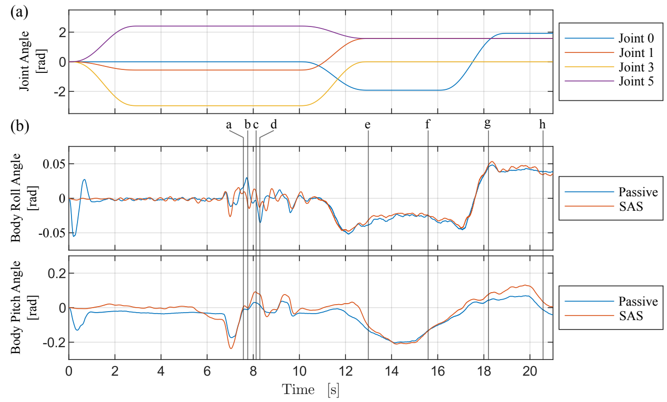

Fig. 5. (a) Motion profiles of the Franka Robot's actively controlled joint throughout the simulation, (b) MBS results for the passive and suggested SAS cases and the 'Cable Channel' and 'Ramp' parts of the ground profile of Fig. 4

TABLE I

SUMMARIZED SIMULATION RESULTS

		Avg. Roll Angle (rad)		Avg. Pitch Angle (rad)	
	Runs	$\mu(Roll)$	σ	$\mu(Pitch)$	σ
a)	Passive	-0.0027	0.0260	-0.0443	0.0661
	SAS	-0.0016	0.0245	-0.0187	0.0817
b)	Passive	0.0026	0.0290	-0.0354	0.0226
	SAS	0.0016	0.0236	-0.0076	0.0221

kinematics, dynamics, and control. Finally, the control of the Franka Robot is also realized in the Simulink model as an open-loop structure in which the pre-calculated joint space trajectories (Fig. 5(a)) are prescribed to each manipulator joint.

*4) **Preliminary Evaluation:*** As the simulation was only a first investigation of the SAS feasibility in the TMM application the control could not be optimized specifically for it. This limited the achievable performance and caused control failure due to instability for the last two obstacles of 4. The results from the MBS are show in Fig. 5(b) and Tab. I. (a) the SAS performs similar to the passive one in the full environment with manipulator motion and ground profile with the only relevant improvement being that the body motion extreme values are sometimes lower, particularly for the roll angle. However, a simulation with a flat ground profile and the full 200s of manipulator motion shown in Fig. 5(a) was also conducted in which the SAS showed a stronger improvement with respect to the passive case as is evident in Table I (b).

III. SYSTEM DESIGN

The core part of the proposed suspension system is an electromechanical variable-stiffness system shown in Fig. 6. This VSS implements a similar concept as [23] and can simultaneously and rapidly change its output stiffness κ and output torque $\tau_{\mathbb{V}}$ in an energy-efficient way.

A. Mechanical Design

The design was created for easy integration into the TMM suspension system (see Section II-B). The arc and drive system is attached to one bogie, while the lower end of the coil spring is connected to the other bogie by a rotational hinge (Fig. 6). Therefore, a relative rotational motion between the two bogies deflects the spring as it changes the output angle of the VSS, which is defined as:

$$\phi = \varphi_{FS} + \varphi_{RS}\,. \tag{9}$$

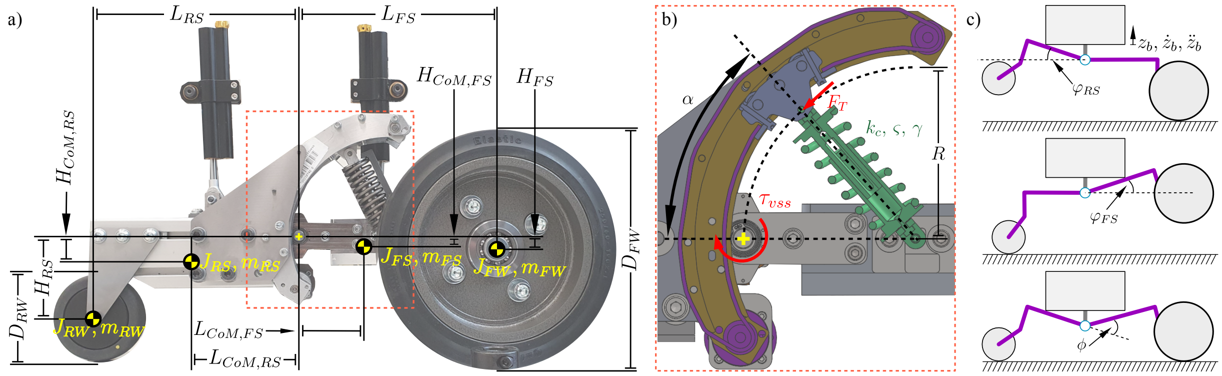

Fig. 6. (a) Developed prototype of the VSS concept testbed and its key geometric variables. (b) CAD section view of the VSS: arc (orange) with cart (blue), spring (green), and drive system (purple). (c) Simplified Diagram of the system to represent the measured φ_{RS}, φ_{FS} and the computed ϕ.

where φ_{FS} and φ_{RS} are the relative angles of the front and rear bogies to the main frame, respectively (See. Fig.6(c)). The principle of stiffness change is similar to that of the system shown in [39] as the stiffness is changed by changing the angle α between the rear bogie and the spring (see Fig. 6). A cart with rollers moves the upper hinge along the arc, with the position described by the angle α. Furthermore, in both systems, a circular arc is used to guide the moving end of the spring, which means that no power is required for stiffness change at zero deflection, making both a variable transmission VSS. Unlike [39], however, a single pre-compressed spring is used here for both positive and negative ϕ. That is why the proposed system can exert an output torque $\tau_{\mathbb{V}} > 0$ at any ϕ and thus fully support the robot weight even at the nominal position $\phi = 0$.

B. Analytical Model

As the VSS uses a standard linear coil spring with known parameters, the equations of the analytical model could be derived using the principle of energy conservation, as the friction and hysteresis losses in the system are assumed to be low. Generally, the variables used are shown in Fig. 6(b). To write the equations compactly, the following two helper variables are introduced:

$$\Lambda = \sin(\alpha + \phi) - \sin(\phi) \,, \tag{10}$$

$$\Gamma = (\cos(\alpha) + \cos(\phi) - 1)^2 + (\sin(\alpha) - \sin(\phi))^2 \,, \tag{11}$$

with the angles α and ϕ being shown in Fig. 6 Then, the rotational stiffness κ of the respective VSS is:

$$\kappa(\Phi, \alpha) = R^2\, k_c \left[\Lambda\Gamma^{-1} + \beta\right] \,, \tag{12}$$

$$\beta = (1 + \varsigma\,\gamma - \sqrt{\Gamma})\sqrt{\frac{1}{\Gamma}}\left(\frac{\Lambda}{\Gamma} + \cos(\alpha+\phi) - \cos(\phi)\right), \tag{13}$$

where R is the arc radius equal to the undeflected joint-to-joint spring length. Furthermore, ς is the maximum compression travel of the spring as a fraction of R while γ is the spring preload travel as a fraction of the actual compression travel $R\varsigma$. Finally, k_c is the linear stiffness of the spring. With this, the output torque $\tau_{\mathbb{V}}$ acting on the bogies (see Fig. 7) is

$$\tau_{\mathbb{V}} = R^2\, k_c\, \Lambda\, (1 + \varsigma\,\gamma - \sqrt{\Gamma})\sqrt{\Gamma^{-1}} \,. \tag{14}$$

Finally, the force F_S that the spring gives in the direction of the stiffness change (see Fig. 6) is:

$$F_S = \tau_{\mathbb{V}} R^{-1} \Lambda^{-1} \left(\sin(\alpha + \phi) - \sin(\alpha)\right) \,. \tag{15}$$

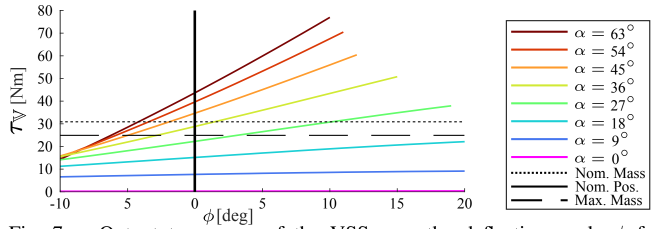

Fig. 7. Output torque $\tau_{\mathbb{V}}$ of the VSS over the deflection angle ϕ for different cart angles α.

Observe that as ϕ approaches 0, F_S diminishes to zero, a feature of the design's kinematics that facilitates energy-efficient operation since F_S has to be overcome by the drive system.

C. Actuation and low-level control

The actuation mechanism plays a crucial role in fulfilling the goals of both high-bandwidth stiffness change and low power consumption. Unlike the system described in [39], the spring angle is altered by exerting force on a cart that moves along the arc, holding the spring in place. Thus the cart is connected to a toothed drive belt that loops around the arc and meshes with two belt gears, the lower of which is driven by a motor-gearbox couple[2]. The belt setup was chosen as it offers significant benefits, including being a cost-effective solution and decreasing the necessary output torque and gearbox size, as the belt transmission functions as a form of gear reduction. Nevertheless, this choice also adapts to the passive use case outlined in Section I that requires the VSS to maintain a stiffness setting with as low motor current as possible. The coulomb friction of the belt reduces the backdrivability of the cart, which helps achieve this goal.

The control of the drive system is defined in two stages. The low-level control is a multilevel cascaded controller that runs and controls the motor-gearbox couple inside the μC. The outer loop is a PID-based position control, the middle loop is a PD-based speed controller, and the inner control loop is a PI-based current control with anti-windup. The measured variables and setpoints are sent to the control PC. The high-level stiffness control is implemented in a Simulink model (Mathworks, MA, USA) hosted in an x64 Ubuntu 20.04 control PC along with the Ethercat Master controller through Etherlab (Ingenieurgemeinschaft IgH, Germany). All

[2]This motor-gearbox couple consists of a 3274G024BP4-6356 BLDC Motor, an AEMT-12/16 L absolute encoder, and a GPT 1:20 gearbox (all Faulhaber GmbH, Germany) and the motor is driven using a custom motor controller board (see [40]) based on an ARM Cortex-M4F microcontroller (μC) connected to the bogie position encoders (see Section IV-A).

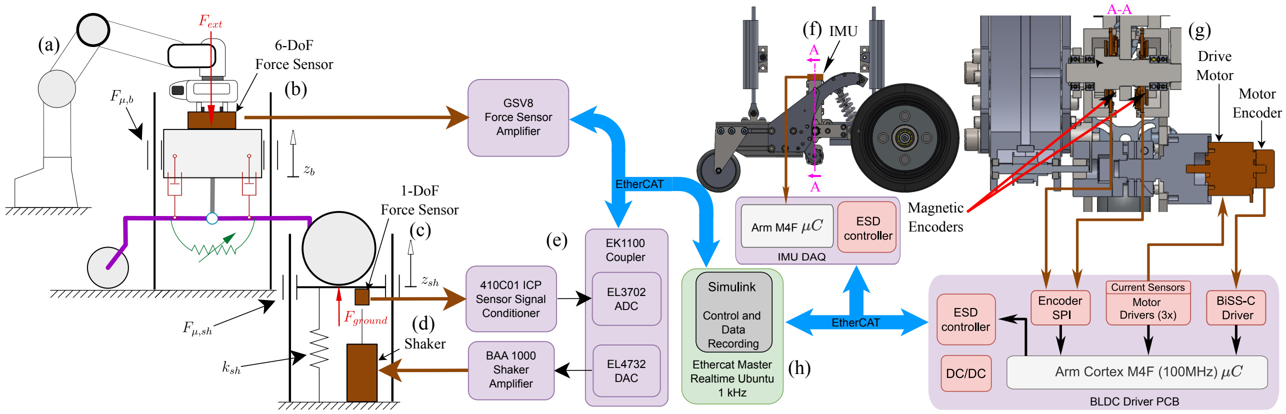

Fig. 8. (a) A Franka robot manipulator exerting $Fext$ to mimic the τ_{man} to the test setup and measured with a (b) 6-DoF Force sensor and its corresponding amplifier. (c) A 1-DoF Force sensor to measure the reaction forces, (d) a Shaker system to emulate the ground forces, and (e) its corresponding signal conditioning electronics. An (f) IMU is located on the top surface of the test setup, and data is acquired via a custom PCB, (g) the actuation motor-gearbox drive and its corresponding electronics, and (h) the main control PC.

additional data acquisition devices are connected to the control PC via EtherCAT at 1 kHz. (see Fig. 8).

IV. Experimental Validation

Confirming the real-world applicability of the proposed concept requires testing a physical prototype. Accordingly, a comprehensive prototype of the VSS was developed and seamlessly integrated into a bogie suspension that, despite being simplified, closely replicates the proposed structure. Efforts were made to precisely replicate the specific boundary conditions relevant to the intended use case, ensuring that the experimental findings are valid and applicable.

A. Experimental Setup

As the TMM is currently conceptual, a simplified test setup encapsulating the critical suspension dynamics was constructed (see Fig. 8). A linear system replicates the right-side bogie of the TMM suspension. Thus, the body of the MB is represented as a mass attached to vertical linear sliders, making the setup a 1-DoF oscillator system. Kinematically, the dimensions are taken from the 'SAM,' while the caster joint of the rear wheel and the torque-controlled drive unit present in SAM are not part of the setup, as these additional DoFs are not the focus point of the study at this point. The system parameters can be found in Tab. II. Generally, the design of the setup reflects the three requirements of the experiment:

- **Representing different body masses**: The mobile base's inertia m_{MB} is simulated by adjusting the body part's mass m_B with additional bolted weights.
- **Evaluating the effect of ground excitations**: To emulate the wheel displacement caused by road obstacles, a TV 51140-M electromagnetic shaker (TIRA GmbH) excites the front wheel. A 208C03 ICP force sensor and a 410C01 ICP Signal Conditioner (PCB Piezotronics) measure the tire-ground contact force.
- **Evaluating the effect of external forces:** Manipulator motion and human interactions are simulated as a vertical force applied by a Franka robot manipulator on top of the 'Body' and measured by a K6D40 MP11 6-DoF force sensor (ME Meßsysteme GmbH).

To adapt to those external excitations, the stiffness adjustment is performed by the servo drive system (Section III-C),

TABLE II

Parameters of the Test Setup

Parameter	Sym.	Unit	Value
Empty Body Mass	m_B	kg	17.73
Front Bogie Mass	m_{FB}	kg	2.27
Front Wheel Mass	m_{FW}	kg	6.36
Rear Bogie Mass	m_{RB}	kg	5.40
Rear Wheel Mass	m_{RW}	kg	0.50
Shaker Support Mass	m_{SH}	kg	2.25
Front Bogie Inertia	J_{FB}	kgm^2	8.69×10^{-3}
Rear Bogie Inertia	J_{RB}	kgm^2	4.43×10^{-2}
Front Wheel Inertia	J_{FW}	kgm^2	1.96×10^{-2}
Body Dynamic Friction	$F_{f,B}$	N	0.16
Shaker Dynamic Friction	$F_{f,SH}$	N	20.98
Rear & Front Bogie Damp.	c_{RB}	Nms/rad	0.16
Vertical Eigenfrequency	$\omega_{0,pas}$	$-$	1.86
Total Damping Ratio	D_{pas}	$-$	0.79
Front Bogie Length	L_{FB}	mm	206.50
Front Bogie Height	H_{FB}	mm	16.00
Rear Bogie Length	L_{RB}	mm	222.00
Rear Bogie Height	H_{RB}	mm	91.00
Current (i) Control	K_p^i	V/A	0.1
	T_i^i	1/s	3.600
	$i^{\max}$	A	$\pm$ 7
Speed $(\dot{\theta})$ Control	$K_p^{\dot{\theta}}$	As/rad	1.0
	$T_d^{\dot{\theta}}$	s	0.1
	$N^{\dot{\theta}}$	$-$	10.0
	$\dot{\theta}^{\max}$	rad/s	$\pm$ 30.0
Position (θ) Control	K_p^{θ}	1/s	20.0
	T_i^{θ}	1/s	10.0

which requires knowledge of the body position, acceleration, and VSS deflection Φ for control. Two single-turn AksIM-2 MB039SPL19BENT00 absolute encoders (RLS d.o.o, Slovenia) located at the bogie hinge measure the angles φ_{FS} and φ_{RS}, respectively. The latter is also used to approximate the body vertical position z_b (see Fig. 6(c)) according to:

$$z_b = -L_{RS}\sin(\varphi_{RS}) - H_{RS}(1 - \cos(\varphi_{RS})) \tag{16}$$

The body acceleration $\ddot{z}_b$, is directly measured with a TDK ICM-42688-P MEMS IMU sensor connected to a custom DAQ system detailed in [41]. The VSS stiffness control, follows the high level controller setup in Section II-C.1, while the low-level control is tuned manually based on setup system identification (see. Tab. II). The manual tunning gives good position control performance with an average settling time of 0.296s for medium steps (0.08 rad) and a maximum settling time of 0.496s for the full operational range (0.413 rad) at full payload (90N).

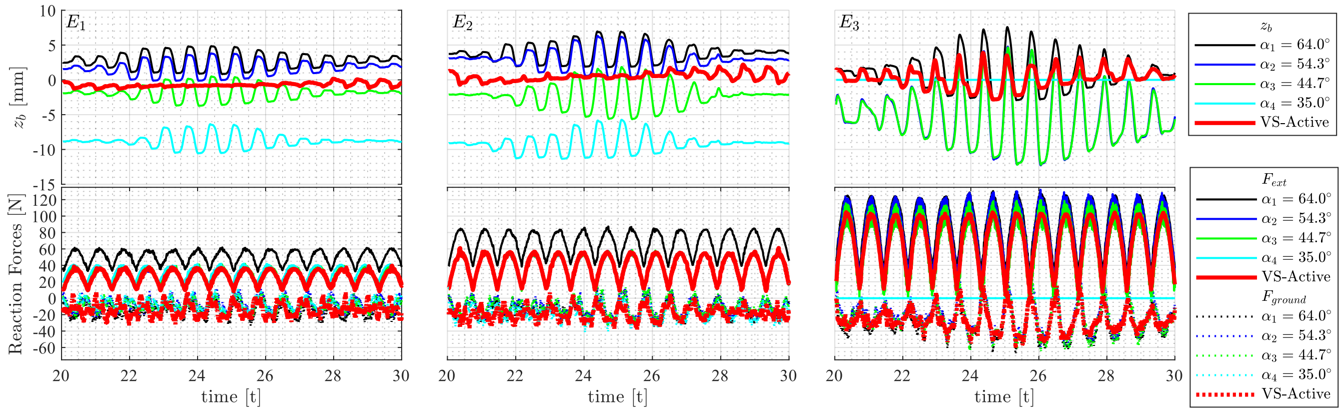

Fig. 9. Experimental results of three cases E_1, E_2 and E_3 specified in Tab. III. The top and bottom rows correspond to the vertical position (z_b) and reaction forces (F_{ext} and F_{ground}), respectively. All cases are evaluated with stiffness values corresponding to four constant α and the suggested SAS.

The proposed system's performance can be effectively evaluated by directly comparing it to alternative solutions. While constructing a fully active system prototype falls beyond the scope of this study, an experimentally replicable passive constant-stiffness system can be achieved by setting the cart angle α and, consequently, the stiffness of the VSS to a constant value. Critical parameters of the VSS and the test setup not listed in Table II should also be considered.

B. Procedure

As the adaptive suspension system is a complex closed-loop system, the effect of individual parameters and excitation on the behaviour cannot be isolated from the impact of others. Therefore, the experiment includes all the assumed use-case effects: Ground profile excitation and external force. The experiment consists of five runs with identical external inputs, one for the adaptive and four for the constant stiffness passive systems ($\alpha_1 = 35.0°$, $\alpha_2 = 44.7°$, $\alpha_3 = 54.3°$, $\alpha_4 = 64.0°$). To simulate the maximum suspension demand, the external force time-signal $F_{ext}(t)$ is not directly derived from the MBS motion input signal frequency, as depicted in Fig. 5-a. Instead, a frequency distinct from the shaker frequency prevents constant synchronization with ground profile changes. The actuator (refer to Section IV-A) is force-controlled to maintain consistency in generating $F_{ext}(t)$ across both passive and controlled runs.

The five runs above for the different stiffness cases repeated for three different $F_{ext}(t)$ cases which are based on the values shown on Tab. III. For each stiffness and F_{ext} case combination, five trials are recorded with a duration of 1 min.

C. Results and Discussion

The results, which were obtained in the experiment are depicted in Fig. 9 and summarized in Tab. IV. For the first two tested cases E_1 and E_2it can be seen that the passive configurations with the higher stiffness values (α_1, α_2) have a better performance compared to the lower stiffness values (α_3, α_4) regarding z_b stability. However, α_1 shows a significant increase in the transferred reaction force, which is not preferred for the system since it could worsen traction and thus safety. These findings would indicate that the best stiffness for the E_1,E_2 scenarios would be α_2. Furthermore by evaluating E_3 we can see that compensating for z_b becomes harder to accomplish for the passive systems: α_1 performance is somewhat worse but still acceptable while α_2 and α_3 have much worse performance while being almost identical to each other. The performance of α_4 could not be recorded as the system reached its motion limits and the Franka robot triggered its safety functions. The transferred reaction forces in E_3 are quite similar for all stiffness settings and within a non acceptable range. Overall, the results for E_3 indicate that α_1 would be the best constant stiffness setting for this case. In all three cases, though, it can clearly be seen that the SAS configuration has a much better z_b stability performance than the passive configurations while also minimizing the reaction forces. Specifically, as seen in Tab. IV, SAS reduces the $\mu(z_b)$ by 60.3%, 53.8% and 43.2% in each respective case, which is a significant improvement. The $\mu(F_{ext})$ is decreased by 19.3%, 1.6% and 9.9% respectively, which is not as significant, but still a good improvement.

TABLE III

PARAMETERS OF THE DIFFERENT EXPERIMENT TEST CASES

Test Case	E_1	E_2	E_3	Units
m_{MB}	24.8	24.8	24.8	kg
m_P/m_{MB}	0.1	0.15	0.2	-
$m_{\mathrm{M}}/m_{\mathrm{MB}}$	0.25	0.35	0.5	-
F_{ext} - Franka Robot Amplitude	22.5	44.1	90.0	N
F_{ext} - Franka Robot Frequency	0.7	0.7	0.7	Hz
F_{ground} - Shaker Voltage	1.5	1.5	1.5	V
F_{ground} - Shaker Frequency	1.5	1.5	1.5	Hz

TABLE IV

SUMMARIZED EXPERIMENT RESULTS

		Avg. Δz_b (mm)		Avg. F_{ext} (N)	
E_n	Runs	$\mu(z_b)$	σ	$\mu(F_{ext})$	σ
1	Passive	4.26	0.47	31.07	6.24
	Semi-Active	1.69	0.09	25.24	1.24
2	Passive	6.12	0.74	41.23	8.33
	Semi-Active	2.83	0.04	40.56	2.85
3	Passive	13.6	2.63	73.61	15.31
	Semi-Active	7.73	0.75	66.34	1.8

V. CONCLUSION AND FUTURE WORK

This study introduces a novel VSS system tailored to TMMs. The feasibility and efficacy of the proposed system are demonstrated through a combination of simulation-based design, experimental validation, and performance analysis. Experimental validation conducted on a physical prototype of the variable stiffness suspension system produced promising results, showcasing its ability to adaptively adjust stiffness in response to external forces and variations in ground profile. The system's semi-active control strategy effectively mitigated undesired body motion caused by external disturbances, enhancing stability and control during TMM operation.

While the experimental results validate the system's performance under controlled conditions, there are opportunities for further optimization and refinement. Future research endeavours could enhance control bandwidth to achieve more significant reductions in body acceleration and conduct additional experimental testing in diverse real-world environments to validate the system's robustness and effectiveness.

As a further goal, reducing body motion acceleration should be the next step in enhancing the system's performance. However, achieving this reduction in body acceleration is likely to be challenging with the proposed system, as the presence of the spring inherently limits the achievable control bandwidth. In the future, using adaptive dampers rather than passive ones, such as magneto-rheological dampers, might offer a solution to overcome this limitation.

Overall, the variable stiffness suspension system holds significant potential for enhancing the mobility, stability, and operational capabilities of TMMs, rendering them more capable and versatile for various applications.

Acknowledgements

The authors would like to thank L. Chen, A. A. Ocal, J. Li, V. Rakčević, R. Kirschner, K. Peper, A. Rahmon, M. Hamad, S. Groß, and J. Ringwald for their valuable support.

References

[1] A. Ajoudani, A. M. Zanchettin, S. Ivaldi, A. Albu-Schäffer, K. Kosuge, and O. Khatib, "Progress and prospects of the human–robot collaboration," *Auton. Robots*, vol. 42, pp. 957–975, 6 2018.

[2] M. Arai and H. Hoshino, "Robot system for removing asbestos sprayed on beams," *28th ISARC, Seoul, Korea*, 2011.

[3] N. GmbH, "Neobotix mmo-500 operating manual," 2023, accessed on 22.05.2023. [Online]. Available: https://www.neobotix-docs.de/hardware/de/manipulators/mmo-500/index.html

[4] A. Dömel, S. Kriegel, M. Kaßecker, M. Brucker, T. Bodenmüller, and M. Suppa, "Toward fully autonomous mobile manipulation for industrial environments," *Int. J. of Adv. Robotic Syst.*, vol. 14, no. 4, p. 1729881417718588, 2017.

[5] K. Zhou et al., "Mobile manipulator is coming to aerospace manufacturing industry," in *Proc. IEEE Int. Symp. on Robotic and Sens. Environ.*, 2014, pp. 94–99.

[6] B. Hamner, S. Koterba, J. Shi, R. Simmons, and S. Singh, "An autonomous mobile manipulator for assembly tasks," *Auton. Robots*, vol. 28, pp. 131–149, 1 2010.

[7] S. Comari et al., "Mobile cobots for autonomous raw-material feeding of automatic packaging machines," *J. of Man. Syst.*, vol. 64, pp. 211–224, 2022.

[8] W. Kim, P. Balatti, E. Lamon, and A. Ajoudani, "Moca-man: A mobile and reconfigurable collaborative robot assistant for conjoined human-robot actions," in *Proc. IEEE Int. Conf. Robot. Autom. (ICRA)*, 2020, pp. 10 191–10 197.

[9] M. Tröbinger et al., "Introducing garmi - a service robotics platform to support the elderly at home: Design philosophy, system overview and first results," *IEEE Robot. and Automat. Lett.*, vol. 6, no. 3, pp. 5857–5864, 2021.

[10] M. C. Yildirim et al., "Development of a collaborative wheeled mobile robot: Design considerations, drive unit torque control, and preliminary result," in *Proc. IEEE Int. Conf. on Robot. and Automat.* IEEE, 2022, pp. 5769–5775.

[11] N. Mansfeld, G. G. Peña, M. Hamad, A. Kurdas, S. Abdolshah, and S. Haddadin, "Global safety characteristics of wheeled mobile manipulators," 2022, pp. 2245–2252.

[12] M. Hamad, A. Kurdas, N. Mansfeld, S. Abdolshah, and S. Haddadin, "Modularize-and-conquer: A generalized impact dynamics and safe precollision control framework for floating-base tree-like robots," *IEEE Trans. on Robot.*, vol. 39, pp. 3200–3221, 8 2023.

[13] R. Suarez, L. Palomo-Avellaneda, J. Martinez, D. Clos, and N. Garcia, "Development of a dexterous dual-arm omnidirectional mobile manipulator," 2018, pp. 126–131.

[14] Robotnik, "Rb-kairos+ 16e technical specifications," 2023, accessed on 22.05.2023. [Online]. Available: https://robotnik.eu/products/mobile-manipulators/rb-kairos/

[15] R. S. Sharp and D. A. Crolla, "Road vehicle suspension system design - a review," *Vehicle Syst. Dynamics*, vol. 16, pp. 167–192, 1 1987.

[16] K. Alipour, S. A. A. Moosavian, and Y. Bahramzadeh, "Dynamics of wheeled mobile robots with flexible suspension: Analytical modelling and verification," vol. 23, 2008.

[17] B. Heißing and M. Ersoy, *Fahrwerkhandbuch*. Vieweg +Teubner Verlag, 2008, pp. 531–536.

[18] W. Bauer, *Hydropneumatische Federungssysteme*, 1st ed., 2008, pp. 136–149.

[19] J. Zhao, P. K. Wong, Z. Xie, C. Wei, and F. He, "Integrated variable speed-fuzzy pwm control for ride height adjustment of active air suspension systems," vol. 2015-July. Institute of Electrical and Electronics Engineers Inc., 7 2015, pp. 5700–5705.

[20] C. Spelta et al., "A new concept of semi-active suspension with controllable damper and spring," in *2009 Eur. Control Conf., ECC 2009*. IEEE, 3 2009, pp. 4410–4415.

[21] M. Hirose, S. Matsushige, S. Buma, and K. Kamiya, "Toyota electronic modulated air suspension system for the 1986 soarer," *IEEE Trans. on Industrial Electronics*, vol. 35, pp. 193–200, 1988.

[22] S. M. Savaresi, C. Poussot-Vassal, C. Spelta, O. Sename, and L. Dugard, *Semi-Active Suspension Technologies and Models*. Elsevier, 2010, pp. 15–39.

[23] A. van der Knaap, "Design of a low power anti-roll/pitch system for a passenger car," *Delft Univ. of Tech,, Vehicle Res. Laboratory, Report*, vol. 89, 1989.

[24] P. J. Venhovens, A. C. V. D. Knaap, and H. B. Pacejka, "Semi-active attitude and vibration control," *Vehicle System Dynamics*, vol. 22, pp. 359–381, 1 1993.

[25] Y. Watanabe and R. S. Sharp, "Mechanical and control design of a variable geometry active suspension system," *Vehicle System Dynamics*, vol. 32, pp. 217–235, 8 1999.

[26] W. J. Evers, A. Teerhuis, A. V. D. Knaap, I. Besselink, and H. Nijmeijer, "The electromechanical low-power active suspension: Modeling, control, and prototype testing," *J. of Dynamic Syst., Measurement and Control, Trans. of the ASME*, vol. 133, 2011.

[27] S. A. Evangelou, "Control of motorcycles by variable geometry rear suspension." IEEE, 2010, pp. 148–154.

[28] O. M. Anubi and C. D. Crane, "Roll stabilisation of road vehicles using a variable stiffness suspension system," *Vehicle Syst. Dynamics*, vol. 51, pp. 1894–1917, 12 2013.

[29] R. Tchamna, M. Lee, and I. Youn, "Attitude control of full vehicle using variable stiffness suspension control," *Optimal Control Appl. and Methods*, vol. 36, pp. 936–952, 11 2015.

[30] P. Múčka, "Simulated road profiles according to ISO 8608 in vibration analysis," *J. of Testing and Eval.*, vol. 46, pp. 405–418, 2018.

[31] J. Lunze, *Regelungstechnik 2*. Springer Berlin Heidelberg, 2013.

[32] T. M. Inc., "Control system toolbox version: 10.11.1 (r2022a)," Natick, Massachusetts, United States, 2022. [Online]. Available: https://www.mathworks.com

[33] J. Clarke, S. Alexander, R. Griffiths, and K. Dare, "Concrete industrial ground floors : a guide to design and construction," 2013.

[34] D. G. U. e.V. (DGUV), "Dguv regel 108-003," 2003.

[35] D. I. für Normung e.V., *Barrierefreies Bauen – Planungsgrundlagen*, din 18040-1:2010-10 ed., 2010.

[36] I. O. for Standardization, *Mechanical vibration — Road surface profiles — Reporting of measured data*, iso 8608:2016(e) ed., 2016.

[37] E. Fiala, "Seitenkräfte am rollenden Luftreifen," *VDI Zeitschrift*, vol. 96, 1954.

[38] F. E. GmbH, "Franka emika panda technical data," 2018, accessed on 26.02.2023. [Online]. Available: https://www.generationrobots.com/media/panda-franka-emika-datasheet.pdf

[39] M. Dezman and A. Gams, "Pseudo-linear variable lever variable stiffness actuator: Design and evaluation." IEEE, 2017, pp. 785–790.

[40] E. P. Fortunic, M. C. Yildirim, D. Ossadnik, A. Swikir, S. Abdolshah, and S. Haddadin, "Optimally controlling the timing of energy transfer in elastic joints: Experimental validation of the bi-stiffness actuation concept," *IEEE Robot. and Automat. Letters*, vol. 8, pp. 8106–8113, 12 2023.

[41] C. M. C. O. Valle, A. Kurdas, E. P. Fortunić, S. Abdolshah, and S. Haddadin, "Real-time imu-based learning: a classification of contact materials," in *2022 IEEE/RSJ Int. Conf. on Intelligent Robots and Syst. (IROS)*, 2022, pp. 1965–1971.